China Instrument and Control Society
Instrumentation
INSTRUMENTATION, Vol. 11, No. 3, September 2024 https://doi.org/10.15878/j.instr.202400174

Article

High Order Total Variational Denoising Algorithm Based on l_0 Overlapping Combination Sparse

Binxin Tang[1], Xianchun Zhou[2,*], Chengcheng Cui[1], Yang Rui[2]

[1] School of Electronic and Information Engineering, Nanjing University of Information Science and Technology, Nanjing 210044, China

[2] School of Artificial Intelligence, Nanjing University of Information Science and Technology, Nanjing 210044, China

[*] Corresponding author email: zhouxc2008@163.com

Abstract: For addressing impulse noise in images, this paper proposes a denoising algorithm for non-convex impulse noise images based on the l_0 norm fidelity term. Since the total variation of the l_0 norm has a better denoising effect on the pulse noise, it is chosen as the model fidelity term, and the overlapping group sparse term combined with non-convex higher term is used as the regularization term of the model to protect the image edge texture and suppress the staircase effect. At the same time, the alternating direction method of multipliers, the majorization–minimization method and the mathematical program with equilibrium constraints were used to solve the model. Experimental results show that the proposed model can effectively suppress the staircase effect in smooth regions, protect the image edge details, and perform better in terms of the peak signal-to-noise ratio and the structural similarity index measure.

Keywords: image denoising; overlapping group sparsity; high-order total variation; l_0-norm; ADMM

Citation: Tang, Binxin, Xianchun Zhou, Chengcheng Cui, and Yang Rui. "High Order Total Variational Denoising Algorithm Based on l0 Overlapping Combination Sparse." Instrumentation 11, no. 3 (September 2024). https://doi.org/10.15878/j.instr.202400174.

1 Introduction

Today, with the rapid development of computer and internet technologies, digital image processing has permeated into our daily lives and work, such as online education, e-commerce, medical diagnostics, video surveillance and so on. Images serve as a crucial medium for information retrieval, characterized by strong visual appeal and high security. However, during the process of image acquisition and transmission, various factors like environmental conditions and system constraints often lead to image degradation, this process is called image degradation[1]. Directly operating on degraded images not only results in the loss of essential image information but also poses risks for subsequent image processing and applications[2]. Therefore, an increasing number of researchers are focusing on enhancing image quality and removing various interference signals, making image denoising a popular and critical technology[3-4].

At the end of the last century, Tikhonov[5] introduced a prior image restoration model based on Tikhonov regularization using the l_2 norm of the image gradient, which improved computational efficiency but suffered from over-smoothing of image details. Addressing this limitation, Rudin, Osher, and others[6] proposed a new image denoising method by measuring image smoothness using the l_1 norm of the gradient, thus pioneering the Total Variation (TV) regularization model. In 2009, Bredies and others[7] introduced the Total Generalized Variation (TGV) model, which, compared to the TV model, possessed properties like rotation invariance and convexity, effectively preserving edges and removing staircase effects. In 2013, the Overlapping Group Sparsity Total Variation (OGSTV) model was first applied to one-dimensional signal Gaussian denoising[8]. In 2015, Liu, Selesnick, and others[9] utilized the sparse characteristics of images, applying OGSTV to image restoration and solving it using the Alternating Direction Method of Multipliers (ADMM) algorithm. In 2019, Adam and colleagues[10] combined high-order non-convex total variation with overlapping group sparsity regularization, where the non-convex high-order

regularization effectively smoothed local image textures while preserving sharp edges. Literature[11] proposed using the TV model with a fidelity term based on the l_0 norm to remove impulse noise, solving the model using proximal ADMM, with experimental results showing that the l_0-norm-based fidelity TV model outperformed the l_1-norm-based fidelity TV model. Yin and others[12] used the l_0-norm-based TV operator as a fidelity term to remove impulse noise, employed overlapping group sparsity regularization to eliminate staircase effects, and used an improved ADMM algorithm for solving, achieving good results. This paper proposes a non-convex pulse noise image denoising algorithm based on the l_0 norm fidelity term, continuing to use non-convex high-order terms as the regularization term of the model to alleviate staircase effects. The improved ADMM algorithm is used for model solving, and it is proven that the model's solution sequence is bounded and converges. Finally, comparing the new model with other mainstream models using peak signal-to-noise ratio and structural similarity index measure, it performs well in subjective visual and objective evaluations, validating the universality and effectiveness of the model in this paper.

2 Related Work

The traditional Total Variation (TV) model can effectively remove noise from images. Depending on the type of noise, different norms are selected as fidelity terms in the model to maximize the denoising effect. The TV model, commonly used for removing Gaussian noise, selects the l_2 norm. However, when this model is used to remove other types of noise, it cannot effectively suppress the outliers caused by the noise. The total variation image denoising model based on the l_1 norm can better remove impulse noise, but it suffers from insufficient penalization, making the model less robust to outliers in the impulse noise. In reference[11], Yuan and others proposed a non-convex image denoising model based on the l_0 norm and introduced an effective proximal alternating direction method (ADM) algorithm. This algorithm equivalently transforms the minimization problem of the l_0 norm into a Mathematical Program with Equilibrium Constraints (MPEC) problem. Experimental results show that this algorithm is more effective than previous penalty decomposition algorithms used for solving the l_0 norm. The image denoising model based on the l_0 norm is represented as follows in formula (1):

$$\min_{u} \| o \odot (Hu - b) \|_0 + \lambda \| Du \|_1 \tag{1}$$

In formula (1), $\lambda>0$ is a regularization parameter used to balance the fidelity term and the regularization term, $\odot$ denotes the standard inner product of matrices. $o \in \{0, 1\}^n$, where $o_i=0$ indicates that the pixel value at position i is an outlier, and $o_i=1$ indicates that the pixel value at position i is a potential outlier. In the subsequent research of this paper, when $b_i=u_{min}$ or $b_i=u_{max}$, it implies that $o_i=0$; otherwise, $o_i=1$.

In reference[12], by reformulating the original dual problem as an MPEC problem, the optimization problem of the l_0 norm is addressed. To simplify the subsequent solving process, the following lemma is introduced to satisfy the l_0 norm in formula (1).

Lemma 1: For any given $x \in \mathbb{R}^n$, formula (2) holds:

$$\begin{aligned} &\| x \|_0 = \min_{v} \langle 1, 1 - v \rangle \\ &s.t. \quad v \odot | x | = 0 \end{aligned} \tag{2}$$

The only solution to formula (2) is:

$$v^* = 1 - sign(|x|) \tag{3}$$

The result of solving Lemma 1 shows that problem (1) can be equivalent to problem (4):

$$\begin{aligned} &\min_{v} \langle 1, 1 - v \rangle + \lambda \| Du \|_1 \\ &s.t. \quad v \odot | o \odot (Hu - b) | = 0 \end{aligned} \tag{4}$$

If u^* is the global optimal solution to problem (1), then (u^*, $1–sign(Hu^*–b)$) is the optimal solution to problem (4); conversely, if (u^*, $1–sign(Hu^*–b)$) is the global optimal solution to problem (4), then u^* is the global optimal solution to problem (1). Since Lemma 1 effectively minimizes the objective function of the norm, it has become a fundamental tool for robust signal and image restoration, facilitating the development of subsequent work in this paper.

3 New Model

3.1 Proposal of High-Order Total Variation Denoising Algorithm Based on l_0 Overlapping Combinatorial Sparsity

In this paper, we propose a pulse denoising model based on overlapping combinatorial sparsity combined with the l_0-TV model as follows:

$$\min_{o \leqslant u \leqslant 1} \| o \odot (Hu - b) \|_0 + \lambda \varphi(Du) + \omega \| D^2 u \|_p^p \tag{5}$$

λ is the parameter controlling the sparsity penalty term. Increasing λ tends to lead the model towards generating sparse solutions, thus better meeting the characteristics of pulse signals. However, setting λ too large may result in excessive sparsity, leading to the loss of some important information. ω is the weight parameter for the l_2 norm penalty term. Increasing ω strengthens the constraint on smoothness, helping to reduce the impact of noise on the signal. However, excessive reliance on smoothness may also lead to the loss of signal details.

The optimization objective of this model is a complex non-convex function, thus iterative algorithms are typically employed for solving it. Common optimization algorithms include gradient descent, coordinate descent, Newton's method, among others. Due

to the presence of both l_0 and l_2 norm terms in the objective function, the optimization problem becomes more challenging. Traditional optimization methods may not be sufficiently effective. Therefore, we need to employ some special techniques or algorithms to solve it, such as heuristic algorithms or approximate optimization methods.

Here, λ>0 is the regularization parameter used to balance the fidelity term and the regularization term. According to reference[12], a limited number of pixel values can be obtained for digital images. Therefore, for ease of discussion and computation, we only consider all images with pixel values within the range [0, 1].

In formula (5), the fidelity term of the model utilizes the l_0 norm term. As widely recognized, the l_0 norm term achieves sparsity by calculating the number of non-zero elements in a vector. The fidelity term $\|o\odot(Hu–b)\|_0$ is used to measure the error between the degraded image and the original image. Since the l_0 norm term calculates the non-zero elements of a vector, it ensures the sparsity of the $o\odot(Hu–b)$ term, making it well-suited for the sparsity property of impulse noise. Therefore, the new model proposed in this paper exhibits stronger robustness to the discrete values of impulse noise.

3.2 Algorithm Solving

Based on Lemma 1, we transform problem (5) into problem (6) as shown below:

$$\begin{aligned} &\min_{o\leqslant u,\ v\leqslant 1} \langle 1,1-v\rangle+\lambda\varphi(Du)+\omega\|D^2u\|_p^p \\ &s.t.\quad v\odot|o\odot(Hu-b)|=0 \end{aligned} \tag{6}$$

By introducing auxiliary variables, we can rewrite equation (6) into the following constrained problem:

$$\begin{aligned} &\min_{o\leqslant u,\ v\leqslant 1} \langle 1,1-v\rangle+\lambda\varphi(x)+\omega\|y\|_p^p \\ &s.t.\quad Du=x,\ D^2u=y,\ Hu-b=z, \\ &v\odot|o\odot z|=v\odot o\odot|z|=0 \end{aligned} \tag{7}$$

Then, by introducing Lagrange multipliers and penalty parameters, we obtain the augmented Lagrangian function as follows:

$$\begin{aligned} &\mathcal{L}_A(u,\ v,\ x,\ y,\ z,\ \pi,\ \pi_a,\ \pi_b,\ \pi_0)= \\ &\langle 1,\ 1-v\rangle+\lambda\varphi(x)+\omega\|y\|_p^p+ \\ &\langle Du-x,\ \pi\rangle+\frac{\beta_1}{2}\|Du-x\|^2+ \\ &\langle D^2u-y,\pi_a\rangle+\frac{\beta_2}{2}\|D^2u-y\|^2+ \\ &\langle Hu-b-z,\pi_b\rangle+\langle Hu-b-z,\pi_b\rangle+ \\ &\frac{\beta_3}{2}\|Hu-b-z\|^2+\langle v\odot o\odot|z|,\ \pi_0\rangle+ \\ &\frac{\beta_4}{2}\|v\odot o\odot|z|\ \|^2 \end{aligned} \tag{8}$$

Where variables π, π_z and π_0 are Lagrange multiplier terms, and $\beta_1, \beta_2, \beta_3$>0 are penalty parameters.

This paper continues to use the ADMM algorithm for solving, and the framework for solving each parameter sub-problem is as follows:

$$\begin{cases} u^{k+1}=\underset{u}{argmin}\langle Du-x^k,\pi^k\rangle+\frac{\beta_1}{2}\|Du-x^k\|^2+\langle D^2u-y^k,\pi_a^k\rangle+ \\ \quad\frac{\beta_2}{2}\|D^2u-y^k\|^2+\langle Hu-b-z^k,\pi_b^k\rangle+\frac{\beta_3}{2}\|Hu-b-z^k\|^2 \\ v^{k+1}=\underset{v}{argmin}\langle 1,1-v\rangle+\langle v\odot o\odot|z^k|,\pi_0^k\rangle+\frac{\beta_4}{2}\|v\odot o\odot|z^k|\ \|^2 \\ x^{k+1}=\underset{x}{argmin}\lambda\varphi(x)+\langle Du^{k+1}-x,\pi^k\rangle+\frac{\beta_1}{2}\|Du^{k+1}-x\|^2 \\ y^{k+1}=\underset{y}{argmin}\omega\|y\|_p^p+\langle D^2u^{k+1}-y,\pi_a^k\rangle+\frac{\beta_2}{2}\|D^2u^{k+1}-y\|^2 \\ z^{k+1}=\underset{z}{argmin}\langle Hu^{k+1}-b-z,\pi_b^k\rangle+\frac{\beta_3}{2}\|Hu^{k+1}-b-z\|^2+ \\ \quad\langle v^{k+1}\odot o\odot|z|,\pi_0^k\rangle+\frac{\beta_4}{2}\|v^{k+1}\odot o\odot|z|\ \|^2 \end{cases} \tag{9}$$

3.3 Subproblem Solving

Formula (9) has transformed the problem into an optimization problem based on the ADMM algorithm framework. Here are the specific solution steps for each parameter:

3.3.1 Subproblem for u

$$\begin{aligned} u^{k+1}=\underset{u}{argmin}\frac{\beta_1}{2}\left\|Du-x^k+\frac{\pi^k}{\beta_1}\right\|^2+\frac{\beta_2}{2}\left\|D^2u-\right. \\ \left.y^k+\frac{\pi_\alpha^k}{\beta_2}\right\|^2+\frac{\beta_3}{2}\left\|Hu-b-z^k+\frac{\pi_b^k}{\beta_3}\right\|^2 \end{aligned} \tag{10}$$

According to the first-order optimality condition, solving problem (10) can be transformed into solving a linear system of equations:

$$\begin{aligned} &(\beta_1D^TD+\beta_2(D^2)^TD^2+\beta_3H^TH)u= \\ &D^T(\beta_1x^k-\pi^k)+(D^2)^T(\beta_2y^k-\pi_a^k)+ \\ &H^T(\beta_3b+\beta_3z^k-\pi_b^k) \end{aligned} \tag{11}$$

Under the periodic boundary conditions of u, both $(D^2)^TD^2$ and H_TH also have block circulant with circulant block (BCCB) structures. Therefore, we can solve it using two-dimensional discrete Fourier transform, and the solution is as shown in formula (12):

$$u^{k+1}=\mathcal{F}^{-1}\left(\frac{\begin{array}{l}\mathcal{F}\left(D^T\right)\odot\mathcal{F}\left(\beta_1x^k-\pi^k\right)+\mathcal{F}\left(\left(D^2\right)^T\right)\odot \\ \mathcal{F}\left(\beta_2y^k-\pi_a^k\right)+\mathcal{F}\left(H^T\left(\beta_3b+\beta_3z^k-\pi_b^k\right)\right)\end{array}}{\begin{array}{l}\beta_1\mathcal{F}\left(D^T\right)\odot\mathcal{F}(D)+\beta_2\mathcal{F}\left(\left(D^2\right)^T\right)\odot \\ \mathcal{F}\left(D^2\right)+\beta_3\mathcal{F}\left(H^TH\right)\end{array}}\right) \tag{12}$$

3.3.2 Subproblem for v

$$v^{k+1}=\underset{v}{argmin}\frac{\beta_4}{2}o\odot z^k\odot z^k\odot v^2+\left(\pi_0^k\odot o\odot|z^k|-1\right)v \tag{13}$$

Thus, formula (13) can be further calculated using projection:

$$v^{k+1} = min\left(1,\ max\left(0, -\frac{\pi_0^k \odot o \odot \left|z^k\right| - 1}{\beta_4 o \odot z^k \odot z^k}\right)\right) \tag{14}$$

Since this subproblem is a projection onto a convex set, it is necessary to ensure that the pixel values of the recovered image are between 0 and 1.

3.3.3 Subproblem for x

According to formula (9), the subproblem for (x) is a problem with overlapping composite sparse terms, so it can be represented as:

$$\begin{aligned} x^{k+1} &= \underset{x}{argmin}\frac{\beta_1}{2}\| x - \left(Du^{k+1} + \frac{\pi^k}{\beta_1}\right)\|^2 + \lambda\varphi(x) = \\ &\underset{x}{argmin}\frac{1}{2}\| x - \left(Du^{k+1} + \frac{\pi^k}{\beta_1}\right)\|^2 + \frac{\lambda}{\beta_1}\varphi(x) \end{aligned} \tag{15}$$

3.3.4 Subproblem for y

$$\begin{aligned} y^{k+1} &= \underset{y}{argmin}\frac{\beta_2}{2}\| y - \left(D^2u^{k+1} + \frac{\pi_a^k}{\beta_2}\right)\|^2 + \omega\| y \|_p^p = \\ &\underset{y}{argmin}\frac{1}{2}\| y - \left(D^2u^{k+1} + \frac{\pi_a^k}{\beta_2}\right)\|^2 + \frac{\omega}{\beta_2}\| y \|_p^p \end{aligned} \tag{16}$$

For ease of solution, let $\tilde{y} = D^2u^{k+1} + \frac{\pi_a^k}{\beta_2}$, then it can be solved as:

$$y^{k+1} = \underset{y}{argmin}\frac{1}{2}\| y - \tilde{y} \|^2 + \frac{\omega}{\beta_2}\| y \|_p^p \tag{17}$$

Applying the IRL1 algorithm, we have:

$$y^{k+1} = \underset{y}{argmin}\frac{1}{2}\| y - \tilde{y} \|^2 + \sum_i t_i \mid y_i \mid \tag{18}$$

Where $t_i = \frac{\omega p}{\left(\left|y_i^k\right| + \epsilon\right)^{1-p}}$. Next, the solution can be obtained using soft thresholding.

3.3.5 Subproblem for z

$$\begin{aligned} z^{k+1} &= \underset{z}{argmin}\frac{\beta_3}{2}\| z - \left(Hu^{k+1} - b + \frac{\pi_b^k}{\beta_3}\right)\|^2 + \\ &\frac{\beta_4}{2}\| v^{k+1} \odot o \odot \mid z \mid + \frac{\pi_0^k}{\beta_4}\|^2 \end{aligned} \tag{19}$$

Expanding formula (19) and removing the constant term, we get:

$$\begin{aligned} z^{k+1} &= \underset{z}{argmin}\frac{1}{2}\left\| z - \frac{\beta_3(Hu^{k+1} - b + \frac{\pi_b^k}{\beta_3})}{\beta_3 + \beta_4(v^{k+1} \odot o)^2}\right\|^2 + \\ &\frac{v^{k+1} \odot o \odot \pi_0^k}{\beta_3 + \beta_4(v^{k+1} \odot o)^2} \odot \mid z \mid \end{aligned} \tag{20}$$

The minimum can be calculated using the following shrinkage operator:

$$z^{k+1} = \frac{\frac{\beta_3\left(Hu^{k+1} - b + \frac{\pi_b^k}{\beta_3}\right)}{\beta_3 + \beta_4\left(v^{k+1} \odot o\right)^2}}{\left|\frac{\beta_3\left(Hu^{k+1} - b + \frac{\pi_b^k}{\beta_3}\right)}{\beta_3 + \beta_4\left(v^{k+1} \odot o\right)^2}\right|} \odot max\left(\left|\frac{\beta_3\left(Hu^{k+1} - b + \frac{\pi_b^k}{\beta_3}\right)}{\beta_3 + \beta_4\left(v^{k+1} \odot o\right)^2}\right| - \frac{v^{k+1} \odot o \odot \pi_0^k}{\beta_3 + \beta_4\left(v^{k+1} \odot o\right)^2}\right)$$

simplify it:

$$\begin{aligned} z^{k+1} &= \frac{Hu^{k+1} - b + \frac{\pi_b^k}{\beta_3}}{\left|Hu^{k+1} - b + \frac{\pi_b^k}{\beta_3}\right|} \\ &\odot max\left(\frac{\beta_3\left|Hu^{k+1} - b + \frac{\pi_b^k}{\beta_3}\right| - v^{k+1} \odot o \odot \pi_0^k}{\beta_3 + \beta_4 v^{k+1} \odot v^{k+1} \odot o}, 0\right) \end{aligned} \tag{21}$$

3.4 Update Variables and Algorithm Framework

After solving each subproblem, it is necessary to update the Lagrange multipliers, as shown in formula (22):

$$\begin{cases} \pi^{k+1} = \pi^k + \beta_1(Du^{k+1} - x^{k+1}) \\ \pi_a^{k+1} = \pi_a^k + \beta_2(D^2u^{k+1} - y^{k+1}) \\ \pi_b^{k+1} = \pi_b^k + \beta_3(Hu^{k+1} - b - z^{k+1}) \\ \pi_0^{k+1} = \pi_0^k + \beta_4(v^{k+1} \odot o \odot \left|z^{k+1}\right|) \end{cases} \tag{22}$$

In conclusion, a non-convex high-order total variation algorithm based on overlapping sparse combinations is obtained. The specific solution steps can be summarized as Algorithm 1:

Algorithm 1: Solving the Optimization Problem

1. Input and parameters λ>0, β_1, β_2, β_3, β_4>0, group size
2. Initialize parameters: u^0=b, k=0 Lagrange operators π, π_a, π_b, π_0
3. Iteration:
Calculate u^{k+1} according to formula (12)
Calculate v^{k+1} according to formula (14)
Calculate x^{k+1} according to formula (15)
Calculate y^{k+1} according to formula (18)
Calculate z^{k+1} according to formula (21)
k=k+1
4. Repeat until the stopping criteria are met

3.5 Analysis of Convergence Proof

This section provides the convergence proof of the proposed algorithm. The algorithm proposed in this chapter is represented by formula (5). Since the fidelity term of the model includes an l_0 norm term, the model solved based on the ADMM framework is also non-convex. Extensive research has been conducted in

references[13-14] on the convergence of non-convex multi-block ADMM, discussing general convergence proof strategies for non-convex nonsmooth minimization problems. This paper also proposes several assumptions regarding the convergence of non-convex nonsmooth minimization algorithms, among which the main methods used to prove the convergence of non-convex nonsmooth algorithms are the Kurdyka–Lojasiewicz (K-L) property and K-L functions. Therefore, if it can be proved that the augmented Lagrangian function is a K-L function, then the non-convex multi-block ADMM algorithm will converge to its critical point, $0\in\partial\mathscr{L}_{\mathrm{A}}$. Based on this, the following lemma is presented:

Lemma 2: Formula (5) is a K-L function.

Proof: The first term of formula (5) is a non-convex term based on the l_0 norm, and since the l_0 norm is a semi-algebraic function, it can be known from reference[15] that this term is a K-L function. The second term of formula (5) is an overlapping sparse combination term, which belongs to the category of convex real-analytic l_2 norms. According to references[16-18], this term also belongs to the category of K-L functions. Formula (5)'s third term, a non-convex term based on the l_p norm, employs the IRL1 algorithm for subproblem resolution. and it has been proven in reference[14] that using IRL1 to solve problems is convergent. Given that the sum of semi-algebraic and real-analytic functions adheres to the K-L property, Formula (5) also meets this criterion, so it's a KL function.

According to Lemma 2, the augmented Lagrangian function (8) also satisfies the K-L property and is a K-L function, so the algorithm proposed in this paper is globally convergent. In addition, the subproblems are either solved exactly or guaranteed to converge, and the OGS subproblems solved based on the MM algorithm also have convergence[19]. Reference[20] also proves the convergence of l_0 norm subproblems. The three parameters are also solved in closed form. Therefore, the convergence of the algorithm proposed in this paper can be fully guaranteed.

4 Experimental Results and Analysis

4.1 Experimental Link and Parameter Setting

This section mainly experiments with the proposed non-convex high-order algorithm based on the l_0 norm. Four standard images (barbara (256×256), starfish (256×256), house (512×512), and couple (512×512)) and four captured images (tower (256×256), road (256×256), cat (512×512), and fireworks (512×512)) from the image dataset Set12 are selected. Simulation experiments are conducted by adding different levels of impulse noise and blur kernels. The original images are shown in Fig.1.

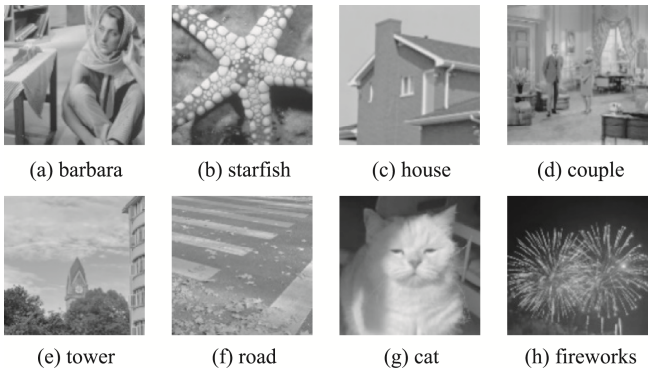

(a) barbara (b) starfish (c) house (d) couple

(e) tower (f) road (g) cat (h) fireworks

Fig.1 The Original Image

For Algorithm 1, the stopping criterion is defined as formula (23):

$$\frac{\| u_{k+1}-u_k \|}{\| u_k \|}\leqslant 1\times10^{-5} \tag{23}$$

In formula (23), u_k and u_{k+1} represent the current and previous iterated images, respectively.

In the experiments, the proposed algorithm is compared with the l_0 total variation model (l_0-TV), the l_0 overlap group sparse total variation model (l_0-OGSTV), and the new model proposed in this paper. Since this paper focuses on the fidelity term of the models, the comparison is mainly based on the selection of fidelity terms, thus choosing the l_0-TV and l_0-OGSTV models.

Next, the experimental parameter settings are discussed. To achieve the optimal image restoration effect, the following parameter ranges need to be determined: regularization parameters λ and ω, group size K in OGSTV, the number of iterations N in the MM algorithm, and the parameter p in the l_p non-convex term.

Firstly, the regularization parameter λ needs to be determined, which plays a crucial role in filtering noise and to some extent determines the quality of image denoise.

Since different levels of impulse noise and blur kernels are added in the experiments, λ is chosen within certain ranges based on experimental experience: $\lambda\in[0.1, 2.1]$ for denoising, $\lambda\in[0.03, 0.5]$ for adding Gaussian blur kernels, and $\lambda\in[0.08, 0.6]$ for adding average blur kernels. Next, we conducted experiments on three images: "tower," "barbara," and "starfish," with the addition of 30% salt-and-pepper noise and a Gaussian blur kernel of size 3*3 and standard deviation 2.

The experimental results are shown in Fig.2. From Fig.2(a), it can be observed that the PSNR value continuously increases when $K\in[1, 3]$; however, when $K\in(3, 10]$, the PSNR value decreases continuously.

Therefore, we conclude that the maximum PSNR value is achieved when K=3. On the other hand, Fig.2(b) illustrates that with the increase of K, the SSIM exhibits a trend of initially increasing and then decreasing, while within the range $K\in[2, 5]$, the SSIM value remains relatively stable. In conclusion, we select K=3 as the optimal group size for our model.

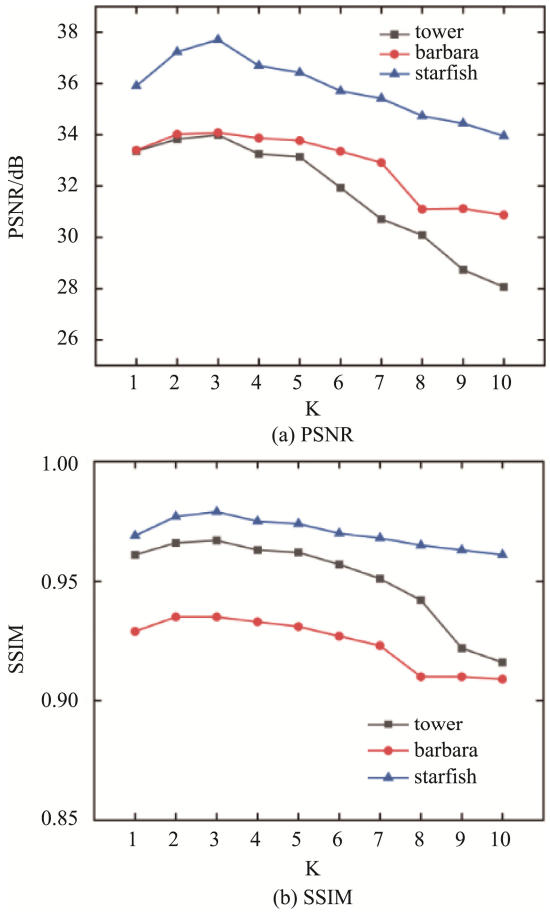

Fig.2 Experimental comparison diagram of parameter K

Next, the value to be determined is the number of internal iterations N in the MM algorithm. When K=3, "tower" and "barbara" images are chosen as experimental images. Additionally, 30% salt and pepper noise is added along with a Gaussian blur kernel of size 3*3 and standard deviation 2. With all other experimental parameters held constant, we investigated the influence of different values of N on the denoising results. Firstly, we observed the variations in PSNR and SSIM, two metrics for evaluating image quality, as N increased. From the experimental results as shown in Table 1, it is evident that as N starts to increase from smaller values, both PSNR and SSIM show improvement, indicating a gradual enhancement in denoising effectiveness. However, once N reaches a certain threshold (N=5), the growth of PSNR and SSIM begins to plateau, and in some cases, minor fluctuations occur, suggesting diminishing returns in terms of image quality improvement with further increments in N.

During the experimentation process, we also noted a significant increase in algorithm runtime as N increased. This is because the increase in internal iteration count implies the algorithm needs to perform more computational steps, leading to an escalation in computational complexity and time consumption. Such growth in time consumption is an important consideration for practical applications, as it directly impacts the efficiency and real-time performance of the algorithm.

Considering the comprehensive analysis above, we can conclude that selecting N=5 as the internal iteration count for subsequent experiments is a reasonable choice. This selection not only ensures a certain level of denoising effectiveness but also controls the algorithm's time consumption within an acceptable range.

During the experiment, to deeply analyze the specific impact of the regularization parameter in the non-convex term on the denoising performance of images, we first understood the different roles of each parameter in image restoration. The regularization parameter λ played a crucial role in initially filtering out image noise, while parameter K, due to its nature, might excessively smooth local regions of the image during noise removal. Additionally, relying solely on the first two terms for image restoration might still leave residual noise spots and blocky artifacts in the image. Hence, introducing the parameter ω aimed to address these issues, aiming to preserve sharp edges and textures in the image to improve the quality of the restored image.

In the experiment, we selected four representative images: "tower," "barbara," "starfish," and "road," and added 30% salt-and-pepper noise and Gaussian blur kernels of size 3*3 and standard deviation 2 to these four images. Keeping the other experimental parameters constant, we studied the influence of different ω values on the denoising effect of images.The experimental results as shown in Fig.3 indicate that the choice of the regularization parameter ω significantly affects the quality of image restoration. From Fig.3(a), we can observe a slight decrease in PSNR as ω gradually increases from 0.1 to 0.6. This may be attributed to a slight decrease in the algorithm's ability to suppress noise as ω increases while preserving the edges and textures of the image. However, when ω continues to increase to the range (0.6, 1], the PSNR value exhibits a significant decrease, indicating that excessively increasing ω values significantly reduce the denoising effect of the image.

Table 1 Experimental data table for parameter N

Image	N	1	5	10	20	50	100	1000
tower	PSNR	33.896	34.204	34.113	34.170	33.876	34.107	34.134
	SSIM	0.961	0.967	0.965	0.966	0.960	0.964	0.966
	TIME	8.962	11.354	13.590	18.138	33.649	57.732	513.710
barbara	PSNR	34.161	34.183	34.011	34.192	34.240	34.088	34.123
	SSIM	0.933	0.936	0.935	0.936	0.937	0.935	0.935
	TIME	8.892	10.775	12.842	17.341	40.422	56.500	515.171

Similarly, Fig.3(b) shows the trend of SSIM with ω values. It is important to note that the statement "when $\omega \in [0.7, 0.6]$" in the original text contains a logical error because the starting value of the interval should be less than or equal to the ending value. Assuming this is a typographical error, we correct it to "when ω gradually decreases from 0.7 to 0.6." Within this range, SSIM shows a significant downward trend, indicating a decrease in the structural similarity of the image and a decrease in image quality.

In conclusion, based on the comprehensive analysis above, we can conclude that setting the range of parameter ω to [0.1, 0.6] is a reasonable choice in this experiment. This range can achieve good denoising effects while preserving the edges and textures of the image and avoiding significant decreases in PSNR and SSIM.

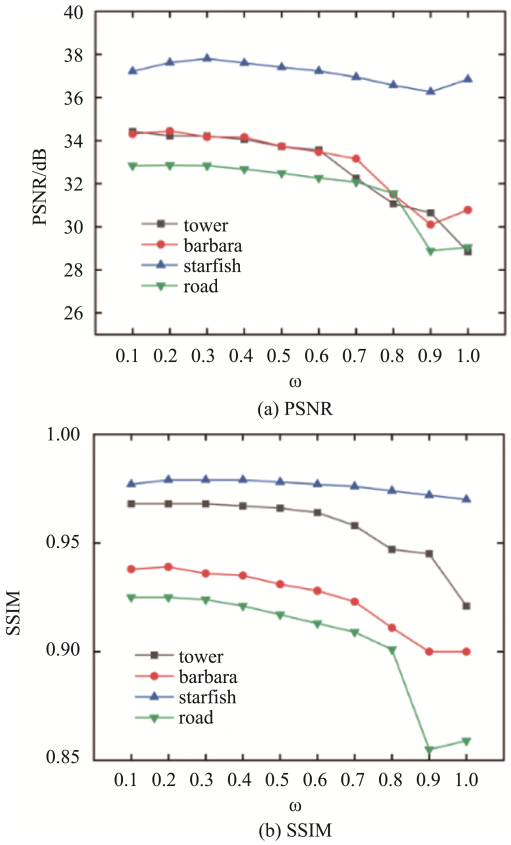

Fig.3 Comparison of PSNR and SSIM values after image denoise under different –values

Another parameter affecting the edge texture of the image is p in the q sub-problem, where p takes values in the range (0, 1] for the l_p norm. Here, three images, "tower," "barbara," and "starfish," were selected. They were subjected to 30% salt and pepper noise and a Gaussian blur kernel of size 3*3 with a standard deviation of 2. The experimental results, as shown in Fig.4, demonstrate a significant influence of the p-value on the quality of image recovery. Firstly, from Fig.4(a), it can be observed that as the p-value gradually increases from 0.3 to 0.7, the PSNR value exhibits a consistent upward trend. This indicates that within this range, as the p-value increases, the denoising effect on the image gradually strengthens, leading to an improvement in image quality. Additionally, it is noteworthy that in Fig.4(b), the SSIM value also shows an increasing trend within this range of p-values, further confirming the enhancement in image quality.

However, it is important to note that although both PSNR and SSIM values increase as the p-value grows, this does not imply that the p-value can be increased indefinitely. Since the p-value is constrained within the range (0, 1] in the definition of the l_p norm, the p-value cannot exceed 1. Furthermore, from the experimental results, it can also be observed that as the p-value approaches 1, the rate of increase in PSNR and SSIM values may slow down or even exhibit a declining trend. This could be attributed to excessively large p-values weakening the algorithm's ability to suppress noise, thus affecting the quality of image recovery.

In summary, based on the analysis of the experimental results, we selected a range of $p \in [0.3, 0.7]$. This range effectively maintains image edges and textures while achieving good denoising results, and it avoids excessive fluctuations in PSNR and SSIM values.

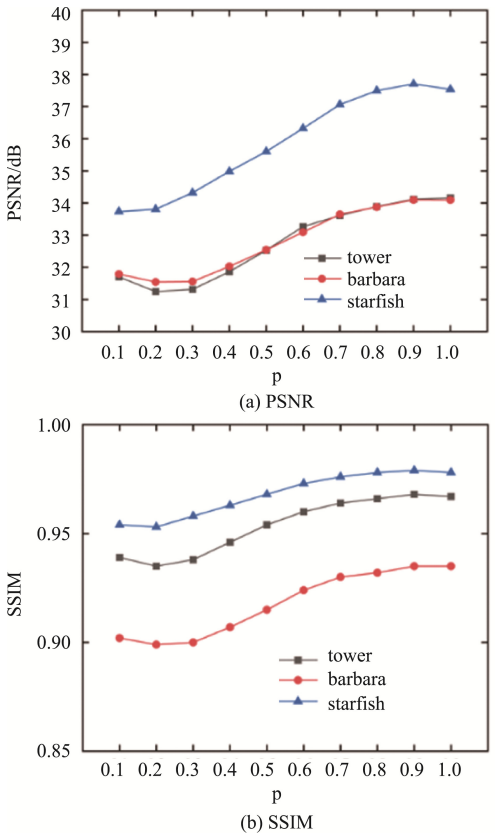

Fig.4 Comparison of PSNR and SSIM values after image denoise under different p-values

4.2 Image Denoising

This section mainly discusses the image denoising performance under impulse noise, with tests conducted on

images containing 30%, 50%, and 70% impulse noise, respectively.

Three sets of images are selected for demonstration, where the first image in each set's first row represents the noisy image, and the rest of the images in the first row depict the denoising effects of various comparative models and our model. The second row in each set shows enlarged local details of the restored images, as illustrated in Figs.5 to 7.

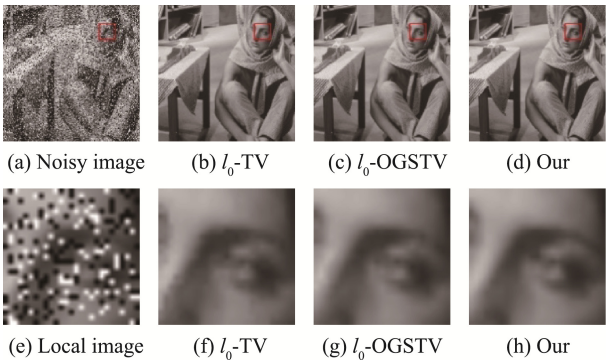

Fig.5 barbara (256×256) Denoising effect image (30%), (a) Noisy image, (b)-(d) Denoising effect of different models, (e) Local image, (f)-(h) Different models denoising local enlarged image

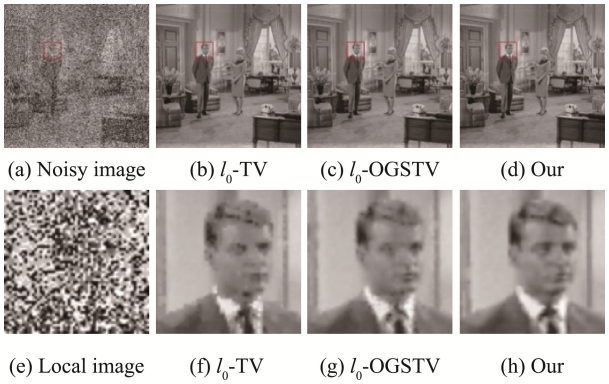

Fig.6 couple (512×512) Denoising effect image (50%), (a) Noisy image, (b)-(d) Denoising effect of different models, (e) Local image, (f)-(h) Different models denoising local enlarged image

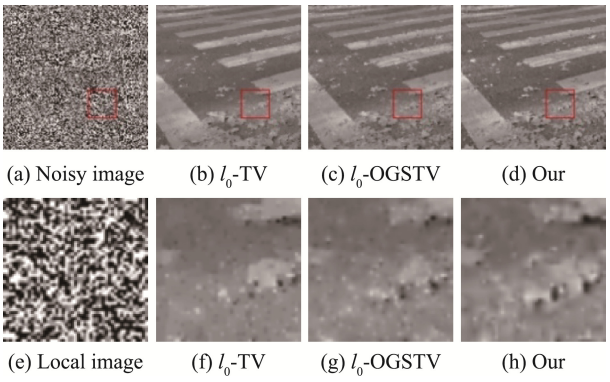

Fig.7 road (256×256) Denoising effect image (70%), (a) Noisy image, (b)-(d) Denoising effect of different models, (e) Local image, (f)-(h) Different models denoising local enlarged image

From Fig.5 to Fig.7, it can be observed that as the noise increases, the difficulty of image restoration also increases. On the whole, the total variation (TV) model based on the l_0 norm can effectively remove image noise, but its ability to handle image edges is insufficient, and the restored image often exhibits a staircase effect. For example, in Fig.6(f), there is significant distortion in the right part of the person's face, and noticeable blocky artifacts appear in the collar area. The contour of the leaves in Fig.7(f) is also not clear. The overlapping sparse total variation model based on the l_0 norm performs better in preserving edge textures compared to the l_0-TV model, but it may result in local oversmoothing of the image. For instance, in Fig.6(g), there is a merging of eye and eyebrow information in the right eye area, leading to incorrect image details. The proposed new model in this paper shows promising results in both denoising and edge texture preservation. For example, in Fig.6(h), even the most challenging facial features are well-preserved with clear facial characteristics, while effectively suppressing the staircase effect.

To further objectively validate the effectiveness of the algorithm in this paper, we evaluate it using PSNR and SSIM metrics, supplemented by the TIME metric. After the experiment, the PSNR, SSIM, and TIME values for the eight groups of experimental images with 30%, 50%, and 70% impulse noise are shown in Tables 2, 3 and 4, respectively.

Table 2 The PSNR (dB) values of different models after denoising

Noise grade	Image	l_0-TV	l_0-OGSTV	Our
30%	barbara	31.869	33.599	33.734
	starfish	31.514	33.200	34.905
	tower	31.083	32.039	32.640
	road	30.408	31.000	31.731
	house	43.390	46.665	49.733
	couple	34.057	35.407	36.345
	cat	37.855	39.618	40.008
	fireworks	29.774	31.797	33.112
50%	barbara	29.247	30.009	30.738
	starfish	28.080	28.882	30.925
	tower	28.245	28.653	29.325
	road	27.736	28.295	28.510
	house	39.807	41.301	46.121
	couple	30.506	31.338	32.453
	cat	35.092	35.796	36.643
	fireworks	26.394	27.420	29.122
70%	barbara	26.541	25.421	27.973
	starfish	24.750	23.888	27.329
	tower	25.797	24.976	26.513
	road	25.270	25.302	25.919
	house	35.594	32.434	39.681
	couple	27.324	26.472	28.896
	cat	32.408	27.344	33.882
	fireworks	23.196	24.701	25.324

Table 3 The SSIM values of different models after denoising

Noise grade	Image	l_0-TV	l_0-OGSTV	Our
30%	barbara	0.943	0.957	0.956
	starfish	0.959	0.971	0.977
	tower	0.958	0.967	0.969
	road	0.917	0.927	0.933
	house	0.992	0.995	0.996
	couple	0.956	0.966	0.969
	cat	0.978	0.984	0.985
	fireworks	0.967	0.978	0.982
50%	barbara	0.898	0.913	0.918
	starfish	0.911	0.927	0.947
	tower	0.914	0.926	0.931
	road	0.844	0.859	0.860
	house	0.979	0.987	0.991
	couple	0.906	0.922	0.932
	cat	0.954	0.965	0.967
	fireworks	0.928	0.927	0.957
70%	barbara	0.827	0.792	0.864
	starfish	0.819	0.771	0.889
	tower	0.837	0.822	0.875
	road	0.729	0.731	0.751
	house	0.949	0.935	0.972
	couple	0.816	0.805	0.858
	cat	0.914	0.785	0.935
	fireworks	0.844	0.795	0.903

Table 4 The TIME values of different models after denoising

Noise grade	Image	l_0-TV	l_0-OGSTV	Our
30%	barbara	1.339	7.252	7.063
	starfish	1.318	7.392	8.095
	tower	1.428	7.474	8.124
	road	1.169	7.537	7.607
	house	6.160	37.965	42.064
	couple	7.228	40.397	48.170
	cat	6.646	35.903	48.090
	fireworks	8.738	43.511	55.457
50%	barbara	1.449	8.084	9.560
	starfish	1.609	8.485	9.311
	tower	1.509	8.001	9.199
	road	1.312	7.781	8.929
	house	7.149	42.860	49.418
	couple	8.094	42.157	52.847
	cat	7.682	39.156	52.776
	fireworks	8.609	44.297	65.828
70%	barbara	2.134	7.998	9.964
	starfish	1.604	8.153	10.331
	tower	1.661	8.363	10.698
	road	1.561	7.901	9.786
	house	8.288	46.621	55.234
	couple	8.811	38.318	57.720
	cat	8.178	44.717	55.457
	fireworks	8.922	39.035	62.924

According to the experimental data in Tables 2 to 4, it is evident that under conditions of 30%, 50%, and 70% impulse noise, the PSNR and SSIM values of our model are significantly higher than those of other comparative models. Moreover, when dealing with different sizes of noisy images, our algorithm achieves higher image evaluation metric values while adding less processing time. Therefore, the new algorithm proposed in this paper for removing impulse noise can produce clear images, preserve edge information, and control algorithm processing time, making it suitable for practical applications.

4.3 Image Deblurring

This section mainly discusses image deblurring using two types of blur kernels: Gaussian blur kernel and average blur kernel. Fig.8 and Fig.9 respectively show the denoising effects of images with 3×3 Gaussian kernel (G) and 3×3 average kernel (A) with a standard deviation of 2, along with 30% added impulse noise. From subjective visual analysis, all three models can effectively remove image noise and blur. However, the l_0-TV model tends to oversmooth local image regions, as seen in Fig.8(b) where the texture details of the cat's neck are smoothed. The l_0-OGSTV model also has deficiencies in handling local details of the image, as evident in Fig.9(g) in the fireworks

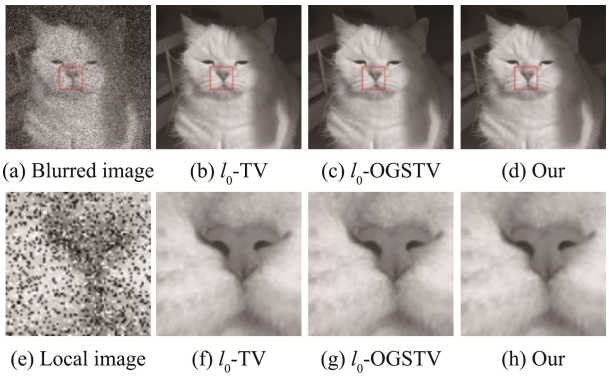

Fig.8 Deblurring effect of cat (512×512) with Gaussian blur (30%), (a) Blurred image, (b)-(d) Denoising effect of different models, (e) Blurred local image, (f)-(h) Enlarged images of denoised local details by different models

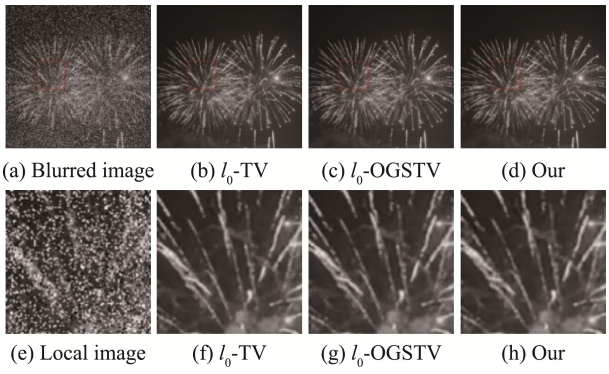

Fig.9 Deblurring effect of fireworks (512×512) with Gaussian blur (30%), (a) Blurred image, (b)-(d) Denoising effect of different models, (e) Blurred local image, (f)-(h) Enlarged images of denoised local details by different models

smoke part. Our new model not only overcomes these shortcomings but also fully considers image structural information, enabling better edge handling and further suppression of the staircase effect.

The comprehensive evaluation of image denoising effects typically involves considering multiple evaluation metrics, including PSNR, SSIM and TIME, among others. These metrics provide information from different aspects, and their combined use can offer a comprehensive understanding of the effectiveness of denoising algorithms. PSNR is one of the classic metrics for assessing image reconstruction quality, measuring the denoising effect by calculating the mean squared error between the original image and the denoised image. A higher PSNR value indicates better denoising effects. However, PSNR only considers pixel-level differences in images, ignoring the nonlinear characteristics of human visual perception. SSIM is another commonly used metric for image quality assessment. It considers not only pixel-level differences but also the structural information of the image and the perceptual characteristics of the human visual system. SSIM values range from -1 to 1, with values closer to 1 indicating greater image similarity, hence better denoising effects. TIME is one of the important metrics for evaluating the practicality of algorithms. Typically, users expect high-quality denoising results while minimizing the processing time of the algorithm. Therefore, it is necessary to consider the trade-off relationship between processing time and denoising effects comprehensively. By considering the results of metrics such as PSNR, SSIM, and processing time, the performance of denoising algorithms can be evaluated from multiple perspectives. The final evaluation should be a conclusion that comprehensively considers both image quality and algorithm efficiency.

Table 5 and Table 6 respectively display the evaluative metrics related to image denoising that are utilized for various models incorporating different blur kernels.

Table 5 The PSNR (dB), SSIM, and TIME values of different models after removing Gaussian blur

Image	Evaluation Index	l_0-TV	l_0-OGSTV	OUR
starfish	PSNR	35.375	36.142	37.677
	SSIM	0.972	0.965	0.978
	TIME	1.664	8.329	9.036
cat	PSNR	39.898	40.362	40.695
	SSIM	0.975	0.970	0.979
	TIME	9.428	32.073	59.344
tower	PSNR	32.898	34.277	34.330
	SSIM	0.975	0.956	0.968
	TIME	9.428	8.400	10.885
fireworks	PSNR	33.953	36.515	37.407
	SSIM	0.982	0.972	0.989
	TIME	8.858	46.652	68.092

Table 6 The PSNR (dB), SSIM, and TIME values of different models after removing Average blur

Image	Evaluation Index	l_0-TV	l_0-OGSTV	OUR
starfish	PSNR	35.673	35.836	37.352
	SSIM	0.971	0.964	0.978
	TIME	1.603	9.385	10.905
cat	PSNR	39.487	39.719	40.479
	SSIM	0.970	0.965	0.978
	TIME	8.911	33.536	61.843
tower	PSNR	32.696	34.178	34.226
	SSIM	0.959	0.950	0.967
	TIME	1.696	8.717	10.805
fireworks	PSNR	34.071	35.698	36.734
	SSIM	0.980	0.968	0.987
	TIME	8.798	43.846	67.677

It is distinctly observable that our innovative new model proposed in this document significantly surpasses other comparative models in terms of Peak Signal to Noise Rati and Structural Similarity Index Measure values.

In summary, the new model proposed in this paper not only excels in subjective evaluations but also outperforms in objective measures compared to the other two conventional models, demonstrating remarkable capabilities in both deblurring and denoising effects.

5 Conclusion

This paper proposes a non-convex high-order image denoising algorithm based on the l_0 norm fidelity term. By improving the fidelity term of the model, the algorithm achieves robustness against outliers in impulse noise while using high-order non-convex terms to preserve fine details of image edge textures. An enhanced ADMM algorithm is employed for solving, where the minimization problem of the l_0 norm is equivalently solved as an MPEC problem. The convergence of the proposed model is also demonstrated, and extensive experiments are conducted to validate the effectiveness of the proposed algorithm. Overall, the experimental results show that the proposed algorithm enhances denoising effectiveness and better preserves image information.

Author Contributions:

Binxin Tang: Took the lead in developing the research questions and overall study design. Conducted extensive raw data collection and led data analysis efforts. The core arguments and main findings of the paper are presented. Wrote most of the manuscript and coordinated the revision.

Xianchun Zhou: Guide the research direction and provide valuable insights at every stage. Approve the final manuscript for submission.

Chengcheng Cui: Additional experiments and validation were carried out. Helps create visual representations of data, such as charts. Participated in the discussion about the interpretation of the study and contributed to refining the conclusions.

Yang Rui: Oversaw the research progress and facilitated communication and collaboration among team members.

Funding Information:

This research was funded by National Nature Science Foundation of China, grant number 61302188.

Data Availability:

The authors declare that the main data supporting the findings of this study are available within the paper and its Supplementary Information files.

Conflict of Interest:

The authors declare no competing interests.

Dates:

Received 21 April 2024; Accepted 17 July 2024; Published online 30 September 2024

References

[1] Zhang B X, Zhu G P, Zhu Z B, et al. (2023). Alternating direction method of multipliers for nonconvex log total variation image restoration. *Applied Mathematical Modelling*, 114, pp.338-359.

[2] Zhou X C, Fan M J. (2021). Four-Directional Total Variation with Overlapping Group Sparsity for Image Denosing. *IEEE Access*, 9, pp.27601-27612.

[3] Deng K, Wen Y W, Li K X, Zhang J. (2024). Hybrid model of tensor sparse representation and total variation regularization for image denoising. *Signal Processing*, (217), pp.109352-109364.

[4] Cui C C. (2023). Research on high order image restoration algorithm based on overlapping combination sparse. *Nanjing University of Information Science and Technology*.

[5] Tikhonov A N, Arsenin V Y. (1977). Solutions of ill-posed problems. *Mathematics of Computation*, 32(144):491-491.

[6] Rudin L I, Osher S, Fatemi E. (1992). Nonlinear total variation based noise removal algorithms. *Physical D Nonlinear Phenomena*, 60(1-4), pp.259-268.

[7] Bredies K, Kunisch K, Pock T. (2010). Total Generalized Variation. *SIAM Journal on Imaging Sciences*, 3(3), pp.492–526.

[8] Selesnick I W, Chen P Y. (2013). Total variation denoising with overlapping group sparsity. *IEEE,* pp.5696-5700.

[9] Liu J, Huang T Z, Selesnick I W, et al. (2015). Image restoration using total variation with overlapping group sparsity. *Information Sciences*, 295, pp.232-246.

[10] Adam T, Paramesran R. (2019). Image denoising using combined higher order non-convex total variation with overlapping group sparsity. *Multidimensional Systems and Signal Processing*, 30(1), pp.503-527.

[11] Yuan G Z, Ghanem B. (2017). ℓ_0TV: A Sparse optimization method for impulse noise image restoration. *IEEE Transactions on Pattern Analysis and Machine Intelligence*, 41(2), pp.352–364.

[12] Yin M M, Adam T, Paramesran R, et al. (2022). An ℓ_0-overlapping group sparse total variation for impulse noise image restoration. *Signal Processing: Image Communication*, 102, pp.116620-116634.

[13] Wang Q S, Han D R. (2023). A generalized inertial proximal alternating linearized minimization method for nonconvex nonsmooth problems. *Applied Numerical Mathematics*,189, pp.66-87.

[14] Chen X J, Zhou W J. (2014). Convergence of reweighted ℓ_1 minimization algorithms for ℓ_2–ℓ_p minimization. *Computation Optimization and Applications,* 59, pp. 47-61.

[15] Hunter D R, Kenneth Lange. (2004). A tutorial on MM algorithms. *American Statistician*, 58, pp.30-37.

[16] Guo C Z, Zhao J, Dong Q L. (2023). A stochastic two-step inertial Bregman proximal alternating linearized minimization algorithm for nonconvex and nonsmooth problems. *Numerical Algorithms*.

[17] Zhao J, Dong Q L, Rassias M T, et al. (2022). Two-step inertial Bregman alternating minimization algorithm for nonconvex and nonsmooth problems. *Journal of Global Optimization*, 84, pp.941-966.

[18] Xu Y Y, Yin W. (2015). A Block Coordinate Descent Method for Regularized Multiconvex Optimization with Applications to Nonnegative Tensor Factorization and Completion. *SIAM Journal on Imaging Sciences*, 6(3), pp.1758-1789.

[19] Ullah H, Amir M, LQBAL M, et al. (2023). De-Noising of Sparse Signals Using Mixture Model Shrinkage Function. *IEEE Access*, (11), pp.7551-7563.

[20] He Y N, Zhu J G, Hao B B. (2023). Hybrid priors based on weighted hyper-Laplacian with overlapping group sparsity for poisson noise removal. *Signal, Image and Video Processing*, (17), pp.2607–2615.